Growth of a Radial Hydraulic Fracture Accounting for the Viscous Fluid Flow in a Rough Cohesive Zone

Liu, D.
EPFL, Lausanne, Switzerland

Lecampion, B.
EPFL, Lausanne, Switzerland

ABSTRACT: We investigate the growth of an axisymmetric hydraulic fracture in an impermeable quasi-brittle material accounting for the presence of a fluid lag. The process zone is simulated using a linear softening cohesive zone model and is characterized by an increased resistance to the fluid flow due to fracture roughness. In the context of a partially-filled cohesive zone, the fracture roughness decreases the tip permeability and further localizes the pressure drop inside the cohesive zone. As a result, a wider fracture opening and higher net pressure are obtained, indicating an increase of the apparent fracture energy. Similar to the linear elastic case, the fracture growth is closely related to a dimensionless parameter ψ which describes the transition nature from the lag-viscosity-toughness regimes. The propagation also depends on the ratio between the in-situ minimum confining stress and the maximum cohesive traction σ_o/σ_T and the type of fluid flow deviation in small rough apertures.

1. INTRODUCTION

Some rocks present a strong non-linear behavior where non-elastic processes such as large plastic deformations or microcracking are no longer negligible. The growth of hydraulic fractures in such rocks may differ from the predictions of linear elastic fracture mechanics (LEFM) theories. Different approaches have been proposed in the literature to account for the inelastic dissipation in the solid. Accounting for the plastic deformation around the fracture tip, Papanastasiou, 1997, 1999; Sarris and Papanastasiou, 2011 report an increase of the fracture apparent energy during the growth of a plane-strain hydraulic fracture. Accounting for the presence of a fluid lag and cohesive forces close to the tip, Rubin, 1993 argues that the cavity in the fluid lag increases with the fracture length and augments the fracture apparent resistance by perturbating the stress field around the tip. These studies show that the rock non-linearity is also responsbile for the larger net propagation pressure (the difference between the fluid pressure and the minimum compressive stress in-situ) in vertical wells of hydraulic fracturing tests (Shlyapobersky, 1985; Shlyapobersky *et al.*, 1988, 1998; Thallak *et al.*, 1993), besides the fracture tortuosity and the additional friction of the wellbore (Palmer and Veatch Jr, 1990; Bunger and Lecampion, 2017). Furthermore, an intrinsical link between the solid non-linearity and the fracture roughness has been revealed through analy-

sis of the fractured surfaces (Ponson, 2016). Elastic and brittle materials present a roughness scaling exponent of around 0.4, and such value is 0.8 for materials with a relatively large process zone (i.e. porceline, silicate glass and granite)(Bonamy and Bouchaud, 2011; Måløy *et al.*, 1992; Schmittbuhl *et al.*, 1993). By increasing the length scale of observation, the process zone size can be determined from the transition of the fracture roughness exponent (Mourot *et al.*, 2005; Bonamy *et al.*, 2006; Ponson *et al.*, 2007; Morel *et al.*, 2008). The length scale at which the roughness exponent transitions from 0.8 to 0.4 indicates the transition from a local non-linear elastic behavior to a overall linear elastic behavior.

Fracture roughness also influences the fluid flow inside the fracture. The fluid flow in a small rough aperture may deviate from the one inside a "smooth" channel, described by Poiseuille's law (cubic law). Such deivation effect is more pronounced in the tip region where the aperture roughness (the difference between two fractured surface roughness) is more significant compared with the fracture opening (Lhomme, 2005; Van Dam and de Pater, 1999). As a result, the hydraulic permeability of the fracture is much reduced (Renshaw, 1995; Zimmerman and Bodvarsson, 1996). The fracture roughness therefore relates the length scale of the solid non-linearity to that of the fluid flow deviation. Such relation has been recognized by Garagash, 2015 when studying the multiphysical tip asymptote
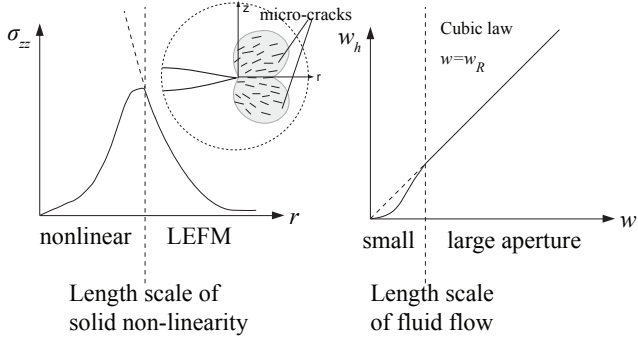
Fig. 1: Schema illustrating the length scale of the solid non-linearity and deviated fluid flow

Fig. 2: Problem description

of a hydraulic fracture in a quasi-brittle medium. The author accounts for a rough cohesive zone with an increased resistance to the fluid flow and reports a higher net pressure, a wider opening and an emergence of an intermediate tip asymptote. In this paper, we aim to understand how such coupled physics affect the propagation of a finite fluid-driven fracture. Based on a model who links the the length-scale of the solid non-linearity to that of the fluid flow deivation, we analyze the growth of a radial hydraulic fracture accounting for the presence of a cohesive zone and fluid lag.

2. PROBLEM DESCRIPTION

We investigate the growth of an axisymmetric fracture in an infinite quasi-brittle impermeable medium. The fracture is driven by an incompressible Newtonian fluid under a constant injection rate Q_o from a point source $r = 0$. Fluid cavitation may occur in the viscous fluid flow and result in a lag between the fluid front and the fracture front. The process zone, associated with the rock non-linearity, is accounted as a part of the fracture and is characterized with an increased resistance to the fluid flow due to the fracture roughness. Solutions of such problem are given by the net fluid pressure $p = p_f - \sigma_o$, (the difference between the fluid pressure p_f and the far-field minimum confining stress σ_o), fracture opening w, fracture radius R, and fluid front radius R_f, which are functions of the position r along the fracture, time t, injection rate Q_o, and other parameters K', E', μ', defined as

$$K' = \sqrt{\frac{32}{\pi}} K_{Ic}, \quad E' = \frac{E}{1 - \nu^2}, \quad \mu' = 12\mu \quad (1)$$

where E is the solid elastic modulus, K_{Ic} fracture effective toughness for quasi-brittle solid, ν Poisson's ratio and μ the
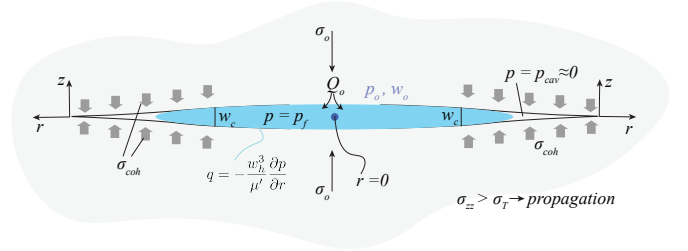
fluid viscosity.

2.1. Cohesive zone model

The process zone is simulated by a linear-softening cohesive zone model. Cohesive tractions apply near the fracture tip and vanish when the fracture opening goes beyond a critical opening w_c. For $w < w_c$, the cohesive stress decreases linearly with the fracture opening, as shown in Fig. 3.

$$\sigma_{coh}(w) = \begin{cases} \sigma_T(1 - w_c) & 0 \le w < w_c \\ 0 & w > w_c \end{cases} \quad (2)$$

where σ_T is the maximum cohesive traction. Using Irwin's equation, the fracture energy thereby denotes

$$G_c = \frac{1}{2}\sigma_T w_c = \frac{K_{Ic}^2}{E'} \quad (3)$$

2.2. Lubrication deivation model

In small rough apertures, e.g. the tip region of a fluid-driven fracture, the fluid flow deviates from Poiseuille's law and results in a decreased permeability. We model such deviation by introducing a friction factor f in Poiseuille's law:

$$w_h^3 = w^3/f, \quad f = 1 + (\frac{w_R}{w})^\alpha, \quad \alpha = 0, 1, 2 \quad (4)$$

where w_h is the hydraulic width of the fracture (for a smooth aperture $w_h = w$), w_R the critical opening characterizes the fluid flow deviation, as illustrated in Fig. 3, which is the same order of magnitude as w_c (Gérard *et al.*, 1996; Garagash, 2015).

For the sake of simplicity, we assume in the following:

$$w_R = w_c \quad (5)$$

The cohesive zone is thereby characterized by a cohesive stress σ_{coh} and an increased resistance to the fluid flow.
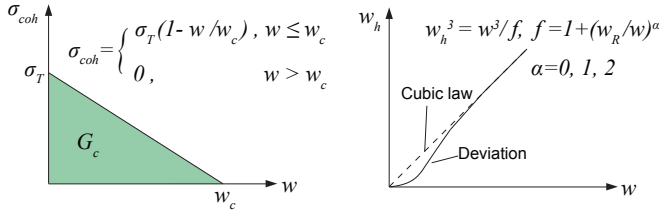
Fig. 3: Problem description

3. GOVERNING EQUATIONS

Elasticity   Deformations of the solid are prescribed by linear elastic equations with the presence of cohesive forces. For a Mode I fracture, the elasticity reduces to a boundary integral equation relating the net pressure $p = p_f - \sigma_o$, cohesive tractions σ_{coh} to the fracture opening w (Zhang *et al.*, 2005; Gordeliy and Detournay, 2011)

$$-\frac{E'}{4\pi}\int_0^R \left[\frac{1}{r'-r}\mathbf{E}(k) + \frac{1}{r'+r}\mathbf{K}(k)\right]\frac{\partial w}{\partial r'}dr' = (p-\sigma_{coh}) \tag{6}$$

where $r \in (0, R)$ represent the position along the fracture. $\mathbf{E}(k)$ and $\mathbf{K}(k)$ denote the complete elliptic integrals, and $k = r/r'$.

Lubrication   Under the assumption of zero leak-off and a negligeble fluid compressibility, the width-averaged mass conservation reduces to

$$\frac{\partial w}{\partial t} + \frac{1}{r}\frac{\partial}{\partial r}(rq) = 0, \quad 0 < r < R_f \tag{7}$$

The local flux q is related to the local pressure gradient under the lubrication approximation through a modified Poiseuille law, considering the deviation effect due to the fracture roughness

$$q = -\frac{w^3}{\mu' f(w, w_R)}\frac{\partial p_f}{\partial r}, \quad 0 < r < R_f \tag{8}$$

Boundary condition   The injection of the fluid is idealized as a point source at the fracture center $r = 0$ with a constant injection rate Q_o. The fracture front $r = R$ is characterized by zero fracture opening.

$$2\pi \lim_{r\to 0} rq = Q_o, \quad w(R,t) = 0 \tag{9}$$

In the fluid lag region, the caviation pressure is null and the fluid front velocity is described by the Stefan equation.

$$p_f(R_f) = 0, \quad R_f \le r < R, \quad \text{and} \quad \dot{R}_f = -\frac{w^2}{\mu' f}\frac{\partial p_f}{\partial r}\bigg|_{r=R_f} \tag{10}$$

Global continuity equation   By integrating the lubrication equation by considering the inlet condition, one gets the global fluid balance,

$$2\pi \int_0^{R_f} rw\,dr = Q_o t \tag{11}$$

Propagation condition   The propagation criteria evaluates the stress component which is perpendicular to the fracture plane σ_{zz}, since the propagation turns into a decohesion process of the material.

$$\sigma_{zz} \ge \sigma_T \tag{12}$$

4. DIMENTIONAL ANALYSIS

We scale the sought quantities $w(r,t)$, $p(r,t)$, $R(t)$ and $R_f(t)$ following the same procedures in (Bunger and Detournay, 2007) .

$$w = W\Omega, \ p = P\Pi, \ R = L\gamma, \ R_f = \vartheta L\gamma_f, \ q = \frac{Q_o}{\vartheta L}\Psi \tag{13}$$

We define respectively the normalized position along the fracture $\xi = r/R$, the fluid front location $\xi_f = R_f/R$, and the cohesive zone length $\xi_{coh} = R_{coh}/R$. By using Irwin's equation (3) (i.e. $K' = 4\sqrt{E'\sigma_T w_c/\pi}$), we get different characteristic scales in three different regimes, representing fluid lag-(O), fluid viscosity-(M) and fracture toughness-(K) dominated regimes respectively, as shown in Table 1

The evolution of a radial hydraulic fracture initiates from a regime where the fluid lag is significant, transitions to the viscosity-dominated regime as the fluid lag coalesces with the fracture front, and reaches the toughness regime due to the increse of geometry at large time. Such evolution depends on the ratio ψ of the transition time from viscosity to toughness regimes t_{mk} and the transition time for the disapperance of the fluid lag t_{om}.

$$\psi = t_{mk}/t_{om} = \frac{E'^{9/2}Q_o^{3/2}\mu'^{3/2}\sigma_o^3}{K'^9} \tag{14}$$

Table 1: Characteristic scales in different scalings. The subscripts o, m, k indicate respectively the lag-, viscosity-, and toughness-dominated regime.

Scaling	O	M	K
L	$L_m \left(\frac{t}{t_{mk}}\right)^{-2/9}$	$L_m = \left(\frac{E'Q_o^3 t^4}{\mu'}\right)^{1/9}$	$L_m \left(\frac{t}{t_{mk}}\right)^{-2/45}$
ϑ	$\left(\frac{t}{t_{mk}}\right)^{2/9}$	1	1
W	W_m	$W_m = \left(\frac{\mu'^2 Q_o^3 t}{E'^2}\right)^{1/9}$	$W_m \left(\frac{t}{t_{mk}}\right)^{-4/45}$
P	P_m	$P_m = \left(\frac{E'^2 \mu'}{t}\right)^{1/3}$	$P_m \left(\frac{t}{t_{mk}}\right)^{2/15}$

$$t_{om} = \frac{E'^2 \mu'}{\sigma_o^3}, \quad t_{mk} = \frac{E'^{13/2} Q_o^{3/2} \mu'^{5/2}}{K'^9} \qquad (15)$$

The dimensional analysis introduces another dimensionless confining stress ratio σ_o/σ_T compared with the linear elastic case. By defining a length scale w_μ characterizing the opening at the fluid front like in (Garagash, 2015), we relate such dimensionless confining stress ratio to the dimensionless ratio ψ. We can also define the length scale of the cohesive zone L_{cooh} and the fluid lag L_λ.

$$w_\mu = \left(\frac{Q_o \mu'}{\sigma_o}\right)^{1/3}, \quad \frac{w_c}{w_\mu} = \frac{\sigma_o}{\sigma_T} \psi^{-2/9} \qquad (16)$$

$$L_{coh} = \frac{E' w_c}{\sigma_T}, \quad L_\lambda = \frac{E' w_\mu}{\sigma_o} = \left(\frac{E'^3 Q_o \mu'}{\sigma_o^4}\right)^{1/3} \qquad (17)$$

w_c/w_μ characterizes the relation between the fluid lag and cohesive zone and describes the penetration degree of the process zone by the fluid. Both a higher confining stress σ_o/σ_T and a smaller ψ ratio result in a higher penetration degree of the cohesive zone: a higher confining stress agrees tends to push the fluid towards the fracture tip and a smaller ψ refers to a faster disappearance of the fluid lag.

Under the assumption of $w_c = w_R$, the fracture roughness will decrease the tip permeability only when the fluid front enters into the cohesive zone. A larger value of w_c/w_μ (larger penetration degree of the cohesive zone by the fluid) indicates a possibly more pronounced viscous dissipation due to the fracture roughness. When $w_\mu \gg w_c$ (often the case of magma flow), the cohesive zone tends to be embedded in the fluid lag and the fracture roughness influences little the fluid flow in the smooth fracture channel. When $w_\mu \ll w_c$ (often the case in hydraulic fracturing), it becomes much easier for fracturing fluid to penetrate the process zone and results in larger energy dissipation in fracturing. The ratio of w_c/w_μ gives an estimation of the interplay between the fluid front and the coehsive zone, yet the penetration degree of the cohesive zone also evolves with time. The propagation initiates from a state where there is no viscous flow in the fracture and the fluid front is embedded in the cohesive zone. As the fracture propagates, the fracture front detaches from the fluid front, and leads to an increase of the fluid lag and a decrease of the penetration degree. Such penetration degree increases again at large time when the fluid lag tends to disappear. The evolution of the interplay between the cohesive zone and the fluid front results in a varying viscous dissipation due to the fracture roughness.

5. NUMERICAL SCHEME

We adopt a fixed regular grid and discretize elasticity and fluid mass conservation by using respectively displacement discontinuity method with piecewise-constant elements and finite volume method. The solution of the hydraulic fracture propagation problem is obtained numerically via a fully implicit scheme. We extend the scheme (CZMLAG) in (Liu and Lecampion, 2019) to the axisymmetric geometry and at the same time account for the roughness-deviated fluid flow. The fluid lag is accounted for using the Elrod-Adams-model at the early stage of the initiation and a level set type algorithm afterwards.

The fluid caviatation is automatically accounted for in the fluid lag initiation algorithm. There is not a clear boundary between the fluid and caviation. A state variable θ characterizes the fluid fraction of the element. Each element can be empty ($p_f = 0$, $\theta = 0$), fully-filled ($p_f > 0$, $\theta = 1$) or partially-filled ($p_f = 0$, $0 < \theta < 1$) by the fluid, all fulfilling Eq. (18).

$$p_f(1 - \theta) = 0 \qquad (18)$$

The level set algorithm instead tracks the evolution of the fluid front position. The fracture is then divided into three parts: the fluid channel where the elements are all fully filled ($p_f > 0$), the fluid lag where there is no fluid at all ($p_f = 0$) and one partially-filled element ($p_f = 0$) where locates the fluid front. The fluid front position is estimated through Eq.(19).

$$R_f = R_f^o + \dot{R}_f \Delta t \qquad (19)$$

where Δt represents the time step and R_f^o the fluid front at the previous time step. The fluid front velocity $\dot{R}_f$ is obtained from the Stefan equation (10). For a given fracture
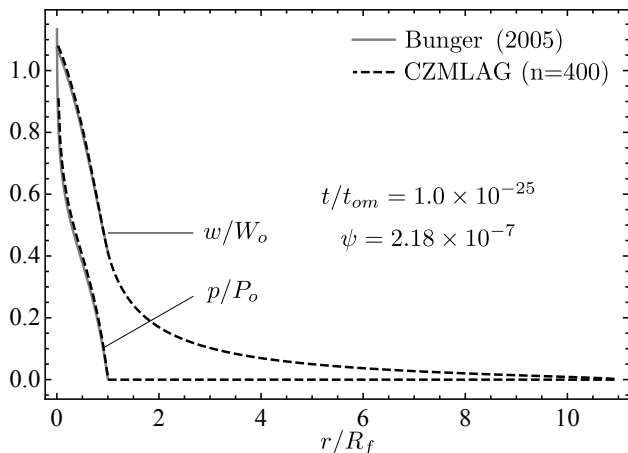
Fig. 4: Benchamark of the numerical scheme for lag-dominated solutions in a linear elastic medium
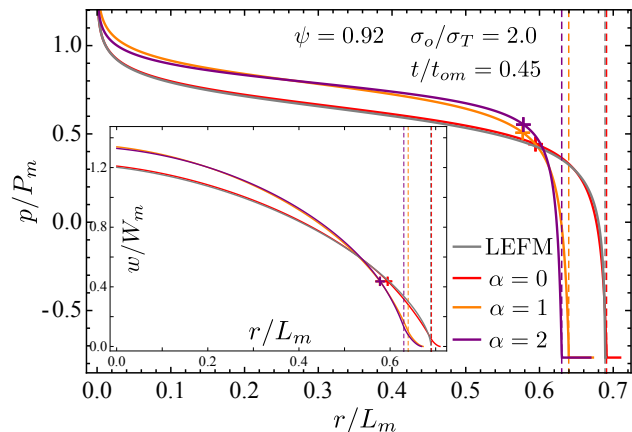

Fig. 5: Comparision of the opening and net pressure. "+" indicates the boundary of the cohesive zone and the vertical dashed lines indicate the fluid front position.

front at time t, the numerical algorithm seeks the fluid front position by using Eq. (10) and Eq.(19) iteratively.

Such fluid-front-tracking algorithm is much more computationally efficient compared to the fluid-lag-intitation algorithm however demands a more accurate estimation of the fluid front position. It may however overestimate the fluid front position and leads to negative fluid pressure near the fluid front. As a result, Eq. (10) no longer captures correctly the fluid front advancing velocity, as pointed out by Gordeliy *et al.*, 2019. In order to better locate the fluid front, we switch to a bi-section algoltham similar to the one in (Gordeliy *et al.*, 2019) when negative fluid pressure occurs. Once the scheme detects a negative fluid pressure in the channel elements (where the elements are fully-filled with fluid) during the sth iteration at the current time step, we utilizes the bi-section algorithm to estimate the fluid front position. We set the fluid front position at the previous time step as the lower bound $R_{fd} = R_f^o$ and the current position $R_f^{(s)}$ as the upper bound $R_{fu} = R_f^{(s-1)}$. As long as the fluid front advances during the fracture growth, the trial fluid front position for the next iteration becomes

$$R_f^{(s+1)} = (R_{fu} + R_{fd})/2 \qquad (20)$$

We iterate on R_f until all fluid pressure in the channel elements remain positive.

5.1. LEFM O-regime benchmark

We benchmark our numerical scheme (CZMLAG) with the semi-analytical solutions of O-regime for a radial fracture

Bunger (2005). We assume that the fracture grows in a linear elastic medium with a toughness of K_{Ic}. The pressure and fracture opening profile at $t/t_{om} = 10^{-25}$ are shown in Fig.4, where W_o and P_o are characteristic scales listed in Table 1.

6. RESULTS

In this section, we first discuss the effect of a smooth cohesive zone and then analyze the effect of the roughness.
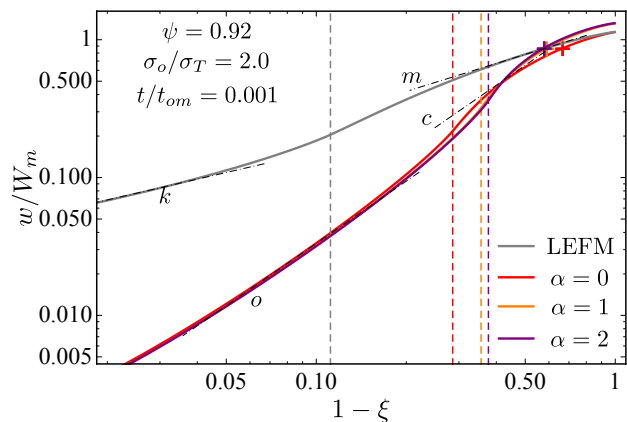

Fig. 6: Comparison of the tip asymptote. Different asymptotes result from the fracture toughness (k-asymptote), viscous fluid flow (m-asymptote), fluid lag (o-asymptote) and cohesive forces (c-asymptote) respectively. "+" indicates the boundary of the cohesive zone and the vertical dashed lines indicate the fluid front position.
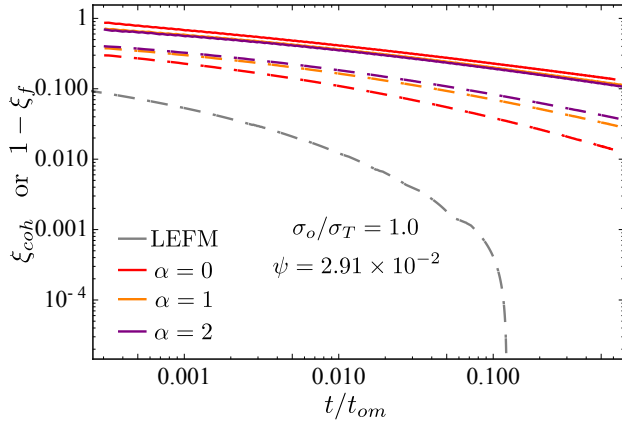
Fig. 7: Evolution of the fraction of the cohesive zone and the fluid lag with time (solid lines-cohesive zone fraction, dashed lines-fluid lag fraction).
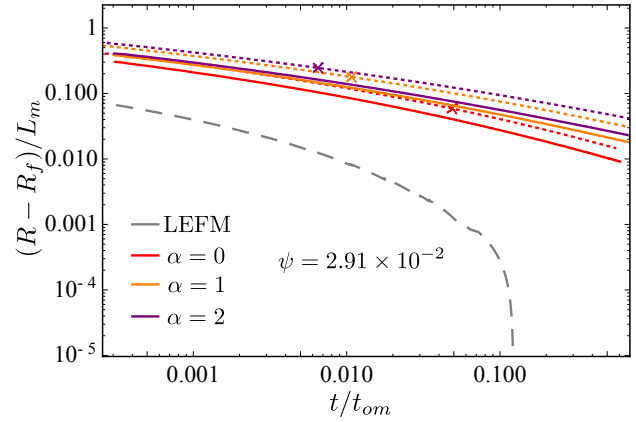

Fig. 8: Effect of σ_o/σ_T on the evolution of the fluid lag with time (dotted lines- σ_o/σ_T = 2.0, solid lines-σ_o/σ_T = 1.0). "×" indicates the time when the fracture radius goes beyond the cohesive zone.

6.1. A smooth cohesive zone

Under the assumption of a smooth coheisve zone, a negative net pressure is formed in the fluid lag region and clamps the fracture tip together with cohesive forces. For a cohesive zone which is partially filled with the injection fluid, such clamping effect pushes the fluid front towards the fracture center and the drop of the net pressure localizes inside the cohesive zone. As a result, a more uniform distribution with a higher value of the net pressure and a wider fracture opening are obatined towards the fracture center compared with the linear elastic case. Such clamping effect in the smooth coheisve zone can be very small as shown in Fig. 5. However, the extent of the fluid lag is much larger thant the predictions of LEFM, as illustrated in Fig. 7 and Fig. 8. More interestingly, the fracture width shows diffrent behaviors in the tip region: the k-asymptote, a tip-asymptote typically for a linear elastic fracture, may be covered by other asymptotes due to the clamping effect as shown in Fig. 6. Such observation agrees with the findings in (Garagash, 2018), where the author reports that the emergence of the k-asymptote would be covered by other asymptotes (o-asymptote representing the fluid lag, c-asymptote the cohesion near the tip, m-asymptote the fluid viscosity) especially for the cases with a relatively large dimensionless confining stress ratio σ_o/σ_T.

The growh of a cohesive hydraulic fracture with time t/t_{om} is closely related to the interplay between the fluid front and the cohesive zone. Such interplay presents an increasing penetration degree at large time and is mainly determined by two parameters: σ_o/σ_T and ψ. A larger di-
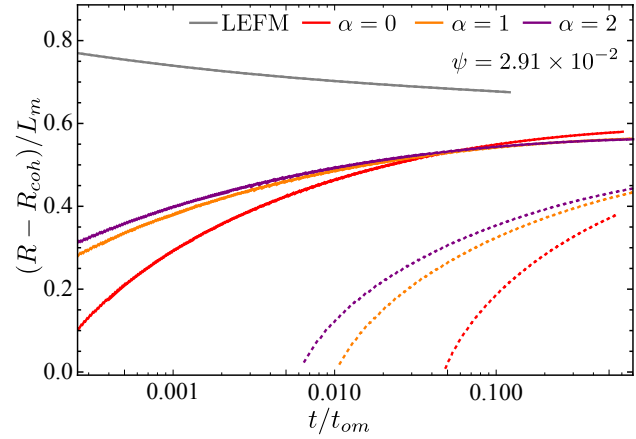
Fig. 9: Effect of σ_o/σ_T on the evolution of the non-cohesive fracture radius with time (dotted lines- σ_o/σ_T = 2.0, solid lines-σ_o/σ_T = 1.0).

mensionless ratio σ_o/σ_T or a smaller ψ often result in a larger penetration degree of the cohesive zone, as demonstrated in Fig. 11 and Fig. 12. As the fracture grows, the cohesive zone takes up less fraction of the fracture as shown in Fig. 7. σ_o/σ_T ratio also determines the time t/t_{om} when the non-cohesive fracture radius begins to develop, as demonstrated in Fig. 9. When the cohesive zone is fully developed at large time, a wider fracture opening is obtained with a higher confining stress ratio σ_o/σ_T, as shown in Fig.10.
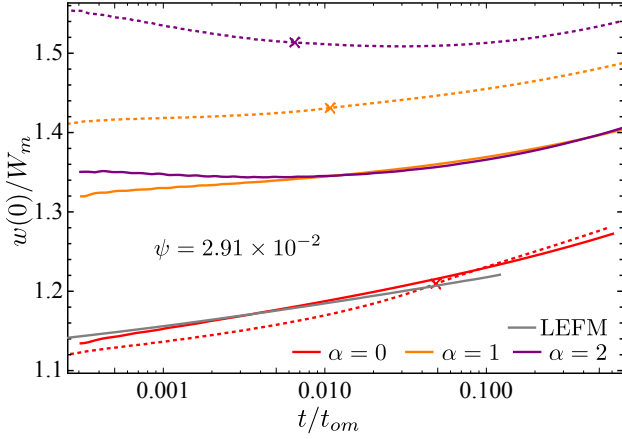
Fig. 10: Effect of σ_o/σ_T on the evolution of the inlet opening with time (dotted lines- $\sigma_o/\sigma_T = 2.0$, solid lines-$\sigma_o/\sigma_T = 1.0$). "$\times$" indicates the time when the fracture length goes beyond the cohesive zone.
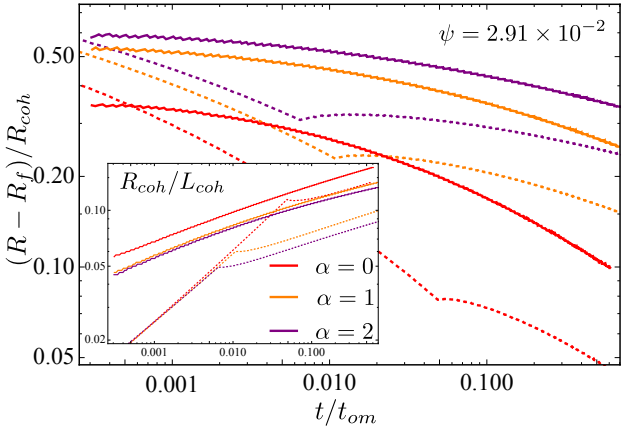

Fig. 11: Effect of σ_o/σ_T on the evolution of the dimensionless cohesive length and the penetration condition of the cohesive zone (dotted lines- $\sigma_o/\sigma_T = 2.0$, solid lines-$\sigma_o/\sigma_T = 1.0$)

6.2. A rough cohesive zone

The fracture roughness decreases the permeability of the fracture tip and makes it more difficult for the fluid to enter into the cohesive zone. As a result, the clamping effect due to cohesive forces in the process zone and the negative net pressure in the fluid lag is further strengthened. The fracture growth presents an increased fracture resistance with a pressure drop localization, a higher net pressure, a wider fracture opening (Fig. 5 and Fig. 10); an enlarged fluid lag (Fig. 7 and Fig. 8), and a lower penetration degree of the cohesive zone (Fig. .11 and Fig. 12).

Such strenghened deviation due to the fracture roughness only takes place when the fluid penetrates into the cohe-
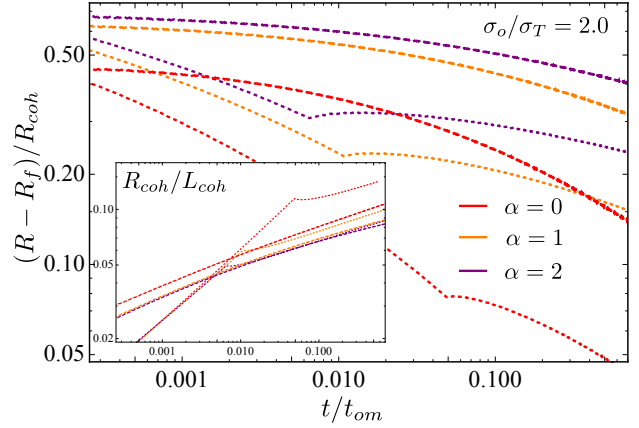

Fig. 12: Effect of ψ on the evolution of the dimensionless cohesive length and the penetration condition of the cohesive zone (dotted lines- $\psi = 2.91 \times 10^{-2}$, dashed lines-$\psi = 0.92$

sive zone (under the assumption of $w_c = w_R$). The effect fracture roughness is closely related to the state of the penetration of the fluid into the cohesive zone. The interplay between the fluid front and the rough cohesive zone evolves with time and depends on three parameters: σ_o/σ_T, ψ and α. For a given α, at a certain dimensionless time t/t_{om}, a higher σ_o/σ_T ratio results in a larger penetration degree of the cohesive zone, as shown in Fig.11, therefore leading to a larger deviation from the linear elastic case. A higher ψ value instead results in a smaller penetration degree, since it indicates a more pronouced effect of the fluid lag at the early stage of the fracture growth where the fluid front probably stays outside the cohesive zone. Fig.13 and Fig.14 presents the effect of roughness on the evolution of the opening profile at different dimensionless time t/t_{om} for the cases with different ψ values. For a larger ψ, the fluid penetration degree is smaller and the influence of the roughness on fluid flow remains very limited. A smaller deviation (smaller increase of inlet fracture opening and smaller change of the fracture opening profile) is obtained compared with the case of a smooth cohesive zone.

7. CONCLUSION

We study the growth of a radial hydraulic fracture in the context of a smooth and a rough cohesive zone, accounting for the presence of a fluid lag. For a smooth cohesive zone, the partial invasion of the cohesive zone results in a localization of the pressure drop within the cohesive zone and a more uniform distribution elsewhere. A higher net pressure
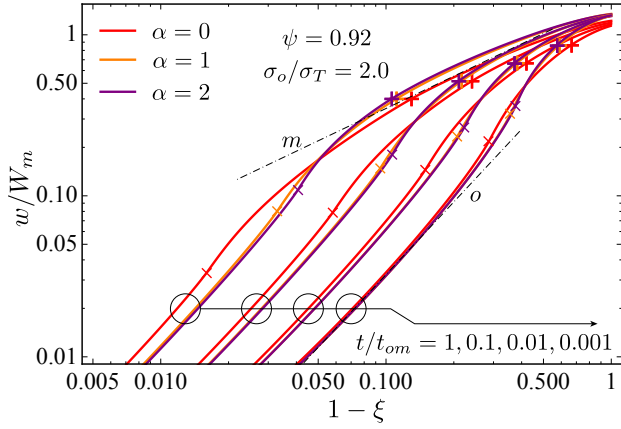
Fig. 13: Evolution of the fracture opening profile with dimensionless time for $\psi = 0.92$ and $\sigma_o/\sigma_T = 2.0$. "+" indicates the boundary of the cohesive zone and "×" indicates the fluid front position.
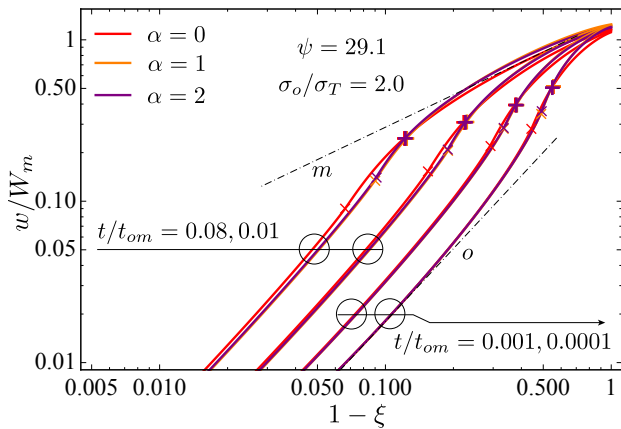

Fig. 14: Evolution of the fracture opening profile with dimensionless time for $\psi = 29.1$ and $\sigma_o/\sigma_T = 2.0$. "+" indicates the boundary of the cohesive zone and "×" indicates the fluid front position.

and wider inlet fracture opening are obtained, though such deviation from the linear elastic case can be very limited. The fracture width near the tip may present quite different behaviors: the classical k-asymptote, which is always obtained in LEFM may be covered by other asymptotes in some cases due to the existence of a process zone. The growth of such a smooth cohesive fracture is closely related to the penetration condition of the coehsive zone by the fluid, which is characterized by two dimensionless parameters, ψ and the dimensionless confining stress ratio σ_o/σ_T. A higher value of t/t_{om}, σ_o/σ_T or a lower value of ψ often indicates a higher penetration degree of the cohesive zone.

Difference between a rough and a smooth cohesive fracture appears only when the fluid front enters into the cohesive zone. The penetration degree significantly determines the increased resistance to the fluid flow due to the fracture roughness. In the context of a partially-filled cohesive zone, the fracture roughness reduces the local permeability near the tip and presents an increased resistance for fracture propagation. The fracture growth with time t/t_{om} depends not only on ψ, σ_o/σ_T but also on the deviation parameter α. For a given rock and injection fluid, the fracture growth then depends on the in-situ minimum confining stress σ_o/σ_T. The viscous dissipation associated with the fluid flow in the rough coheisve zone is of course related to σ_o/σ_T. Its evolution with time needs further investigation.

REFERENCES

1. Bonamy, D. and Bouchaud, E., 2011. Failure of heterogeneous materials: A dynamic phase transition?, *Phys. Rep.*, 498 (1), 1–44.

2. Bonamy, D., Ponson, L., Prades, S., Bouchaud, E., and Guillot, C., 2006. Scaling exponents for fracture surfaces in homogeneous glass and glassy ceramics, *Phys. Rev. Lett.*, 97 (13), 135504.

3. Bunger, A. and Lecampion, B., 2017. Four critical issues for successful hydraulic fracturing applications, CRC Press, Chapter 16.

4. Bunger, A.P., 2005. *Near-surface hydraulic fracture*, Ph.D. thesis, University of Minnesota.

5. Bunger, A.P. and Detournay, E., 2007. Early-time solution for a radial hydraulic fracture, *J. Eng. Mech.*, 133 (5), 534–540.

6. Garagash, D.I., 2015. How fracking can be tough, IMA Workshop Hydraulic Fracturing Modeling and Simulation to Reconstruction and Characterization, University of Minnesota.

7. Garagash, D.I., 2018. What good is linear elastic fracture mechanics in HF?, *BIRS Hydraulic Fracturing Workshop*, Banff.

8. Gérard, B., Breysse, D., Ammouche, A., Houdusse, O., and Didry, O., 1996. Cracking and permeability of concrete under tension, *Mater. Struct.*, 29 (3), 141–151.

9. Gordeliy, E., Abbas, S., and Peirce, A., 2019. Modeling nonplanar hydraulic fracture propagation using the XFEM: An implicit level-set algorithm and fracture tip asymptotics, *Int. J. Solids Struct.*, 159, 135–155.

10. Gordeliy, E. and Detournay, E., 2011. A fixed grid algorithm for simulating the propagation of a shallow hydraulic fracture with a fluid lag, *Int. J. Numer. Anal. Methods Geomech.*, 35 (5), 602–629.

11. Lhomme, T.P.Y., 2005. *Initiation of hydraulic fractures in natural sandstones*, TU Delft, Delft University of Technology.

12. Liu, D. and Lecampion, B., 2019. Propagation of a plane-strain hydraulic fracture accounting for the presence of a cohesive zone and a fluid lag, *in: 53rd US Rock Mechanics/Geomechanics Symposium*, ARMA.

13. Måløy, K.J., Hansen, A., Hinrichsen, E.L., and Roux, S., 1992. Experimental measurements of the roughness of brittle cracks, *Phys. Rev. Lett.*, 68 (2), 213.

14. Morel, S., Bonamy, D., Ponson, L., and Bouchaud, E., 2008. Transient damage spreading and anomalous scaling in mortar crack surfaces, *Phys. Rev. E*, 78 (1), 016112.

15. Mourot, G., Morel, S., Bouchaud, E., and Valentin, G., 2005. Anomalous scaling of mortar fracture surfaces, *Phys. Rev. E*, 71 (1), 016136.

16. Palmer, I.D. and Veatch Jr, R.W., 1990. Abnormally high fracturing pressures in step-rate tests, *SPE Prod. Eng.*, 5 (03), 315–323.

17. Papanastasiou, P., 1997. The influence of plasticity in hydraulic fracturing, *Int. J. Fract.*, 84 (1), 61–79.

18. Papanastasiou, P., 1999. The effective fracture toughness in hydraulic fracturing, *Int. J. Fract.*, 96 (2), 127–147.

19. Ponson, L., 2016. Statistical aspects in crack growth phenomena: how the fluctuations reveal the failure mechanisms, *Int. J. Fract.*, 201 (1), 11–27.

20. Ponson, L., Auradou, H., Pessel, M., Lazarus, V., and Hulin, J.P., 2007. Failure mechanisms and surface roughness statistics of fractured fontainebleau sandstone, *Phys. Rev. E*, 76 (3), 036108.

21. Renshaw, C.E., 1995. On the relationship between mechanical and hydraulic apertures in rough-walled fractures, *J. Geophys. Res. Solid Earth*, 100 (B12), 24629–24636.

22. Rubin, A.M., 1993. Tensile fracture of rock at high confining pressure: implications for dike propagation, *J. Geophys. Res. Solid Earth*, 98 (B9), 15919–15935.

23. Sarris, E. and Papanastasiou, P., 2011. The influence of the cohesive process zone in hydraulic fracturing modelling, *Int. J. Fract.*, 167 (1), 33–45.

24. Schmittbuhl, J., Gentier, S., and Roux, S., 1993. Field measurements of the roughness of fault surfaces, *Geophys. Res. Lett.*, 20 (8), 639–641.

25. Shlyapobersky, J., 1985. Energy analysis of hydraulic fracturing, *in: The 26th US Symposium on Rock Mechanics (USRMS)*, Rapid City, South Dakota: ARMA.

26. Shlyapobersky, J., Issa, M.A., Issa, M.A., Islam, M., Dudley, J.W., Shulkin, Y., and Chudnovsky, A., 1998. Scale effects on fracture growth resistance in poroelastic materials, *in: SPE Annual Technical Conference and Exhibition*, SPE.

27. Shlyapobersky, J., Wong, G., and Walhaug, W., 1988. Overpressure calibrated design of hydraulic fracture stimulations, *in: SPE Annual Technical Conference and Exhibition*, SPE.

28. Thallak, S., Holder, J., and Gray, K., 1993. The pressure dependence of apparent hydrofracture toughness, *in: The 34th US Symposium on Rock Mechanics (USRMS)*, Madison, Wisconsin: ARMA.

29. Van Dam, D. and de Pater, C., 1999. Roughness of hydraulic fractures: The importance of in-situ stress and tip processes, *in: SPE Annual Technical Conference and Exhibition*, SPE.

30. Zhang, X., Jeffrey, R., and Detournay, E., 2005. Propagation of a hydraulic fracture parallel to a free surface, *Int. J. Numer. Anal. Methods Geomech.*, 29 (13), 1317–1340.

31. Zimmerman, R.W. and Bodvarsson, G.S., 1996. Hydraulic conductivity of rock fractures, *Transp. Porous Media*, 23 (1), 1–30.